Molecular architectures of iron complexes for oxygen reduction catalysis—Activity enhancement by hydroxide ions coupling

Poe Ei Phyu Win[a,1], Jiahui Yang[a,1], Shuwang Ning[b,1], Xiang Huang[c,2] (ID), Gengtao Fu[b] (ID), Qiming Sun[a,d], Xing-Hua Xia[e,2] (ID), and Jiong Wang[a,d,2] (ID)

Developing cost-effective and high-performance electrocatalysts for oxygen reduction reaction (ORR) is critical for clean energy generation. Here, we propose an approach to the synthesis of iron phthalocyanine nanotubes (FePc NTs) as a highly active and selective electrocatalyst for ORR. The performance is significantly superior to FePc in randomly aggregated and molecularly dispersed states, as well as the commercial Pt/C catalyst. When FePc NTs are anchored on graphene, the resulting architecture shifts the ORR potentials above the redox potentials of $Fe^{2+/3+}$ sites. This does not obey the redox-mediated mechanism operative on conventional FePc with a Fe^{2+}–N moiety serving as the active sites. Pourbaix analysis shows that the redox of $Fe^{2+/3+}$ sites couples with HO^- ions transfer, forming a HO–Fe^{3+}–N moiety serving as the ORR active sites under the turnover condition. The chemisorption of ORR intermediates is appropriately weakened on the HO–Fe^{3+}–N moiety compared to the Fe^{2+}–N state and thus is intrinsically more ORR active.

molecular electrochemistry | molecular assembly | collective effects | redox-mediated mechanism | oxygen reduction reaction

Low-temperature fuel cells and metal–air batteries represent promising clean energy output systems and the efficiency of energy utilization largely relies on the cathodic electrochemical process of oxygen reduction reaction (ORR) owing to its sluggish kinetics (1–3). Although platinum (Pt) and Pt-based materials have been commonly applied as cathodic electrocatalysts, their applications are limited by high cost and low stability (4, 5). To search for non-noble electrocatalysts with outstanding ORR performance is a long-term objective for the large-scale application of fuel cells or batteries (6, 7). Particularly, transition metal phthalocyanine attracts increasing attention for its facile synthesis and being made of non-noble elements (8). Among various metal species, FePc (iron phthalocyanine) exhibits the optimal performance because its d orbitals are partially filled resulting in appropriate chemisorption of O_2 (9, 10). To operate electrocatalysis of ORR, it commonly adopts the redox-mediated mechanism, which can be inspired from natural enzymes, such as cytochrome c (cyt c)/cyt c oxidase, having analogous Fe coordination spheres (11–13). Namely, the reduction of Fe^{3+} into Fe^{2+} states leaves open chemisorption sites for O_2 and commence the electrocatalysis. The ORR overpotential is thus dictated by the redox of $Fe^{3+/2+}$ pair (10, 14). Such a mechanism is extended to many other molecular electrocatalytic systems, while it brings an intrinsic flaw that the electrocatalytic performance can be limited by the redox thermodynamics of molecular complexes. Recently, Surendranath et al. (15, 16). proposed that through intense electron coupling between molecular complexes and graphite, it generates continuous electron energy level at the interface of two species and eliminates the redox behaviors of complexes converting them into metallic-like catalytic properties. Very rapid catalytic kinetics of hydrogen evolution reaction was observed. While as far as we know, there are few studies reporting to break the limitation of redox-mediated mechanism for ORR and other electrocatalytic reactions.

Except for the structural tuning of complexes at the single molecular level, the aggregate states are well known to have significant impacts on tuning the electronic properties of molecules through intermolecular interactions (e.g., H-bond, π–π, and C–H...π interactions), as well as changing intramolecular bond movements (17, 18). Recent studies show that the aggregate states could also affect the electrocatalytic performance. For instance, Sun et al (19). suggested that a face-to-face assembly resulted in FePc molecules approaching each other, generating dual Fe centers. In their density functional theory (DFT) calculations, the authors found that O_2 adsorbed within the dual Fe centers forming a Fe–O–O–Fe bridging configuration, which is distinct from that O_2 adsorbed onto a single Fe site with a linear geometry. The bridging configuration could be energetically favored to cleave O_2 compared to the case of linear adsorption. However, the molecular aggregation could affect the interfacial electron transfer emerged in electrochemical reactions. In a study of electrocatalytic CO_2 reduction, Berlinguette et al. (20). showed that ongoing

Significance

Iron phthalocyanine (FePc) has been utilized for catalyzing oxygen reduction reaction (ORR) as inspired by natural enzymes. The assembled FePc with relatively ordered nanotube morphology shows superior electrocatalytic ORR performance compared to FePc in a freely aggregated state and a molecularly dispersed state. The nanotube architecture shifts the ORR potentials above the redox potentials of $Fe^{2+/3+}$ sites. This does not obey the redox-mediated mechanism operative on conventional FePc with a Fe^{2+}–N moiety serving as the active sites. Instead, the electrocatalysis operates on a highly oxidized FePc ligating additional HO^- ions, namely, a HO–Fe^{3+}–N moiety. Such a moiety is intrinsically more active than the Fe^{2+}–N moiety.

[1]P.E.P.W., J.Y., and S.N. contributed equally to this work.

[2]To whom correspondence may be addressed. Email: huangx8@sustech.edu.cn, xhxia@nju.edu.cn, or wangjiong@suda.edu.cn.

from an uniformly dispersed state to a randomly aggregated state, the redox of CoPc molecules turned to be difficult as verified by operando Raman spectra, and thus, a low oxidation active state of CoPc was not generated, which blocked CO_2 reduction. This indicates that aggregated molecules can be poorly conductive as the intermolecular electrical resistance can be significant without appropriate linkages (21).

In this work, we report the assembly of FePc molecules into relatively ordered nanotube morphology. This structure shows high structural stability and electrical conductivity in both inner- and outer-sphere electron transfer (ISET/OSET) pathways. Importantly, such FePc nanotubes (NTs) exhibit superior ORR performance compared to FePc in a random aggregated state and a molecularly dispersed state. We found that the ORR mechanism varies with the aggregate states of FePc. The molecularly dispersed FePc follows the classical redox-mediated mechanism, and the random aggregates do not exhibit any redox response of Fe sites that ORR should directly occur on Fe^{2+}–N sites. In contrast, the redox response of Fe sites is significant in FePc NTs, and the ORR

potential shifts above the redox potential of Fe sites. The electro-catalysis operates on a highly oxidized FePc ligating additional HO^- ions, namely, a $HO–Fe^{3+}–N$ moiety, according to the Pourbaix analysis. Such a moiety is verified as intrinsically more active than the Fe^{2+}–N state.

Results and Discussions

Structural Analysis. The synthesis of FePc NTs followed an ethylene glycol-assisted solvothermal method (22) and was loaded onto reduced graphene oxides (rGO) for facilitation of electron transport and increasing the utilization efficiency of FePc NTs. The resultant sample is denoted as FePc NTs-rGO (the details are provided in *SI Appendix*). Inductively coupled plasma (ICP) measurements indicate that the Fe contents of FePc NTs-rGO are at 1.2×10^{-6} mol mg^{-1} magnitude (*SI Appendix*, Table S1). The scanning and transmission electron microscopy (SEM/TEM) images show that the as-synthesized FePc NTs have the diameter of 100 to 400 nm with length of 2 to 6 μm (Fig. 1*A* and *SI Appendix*,
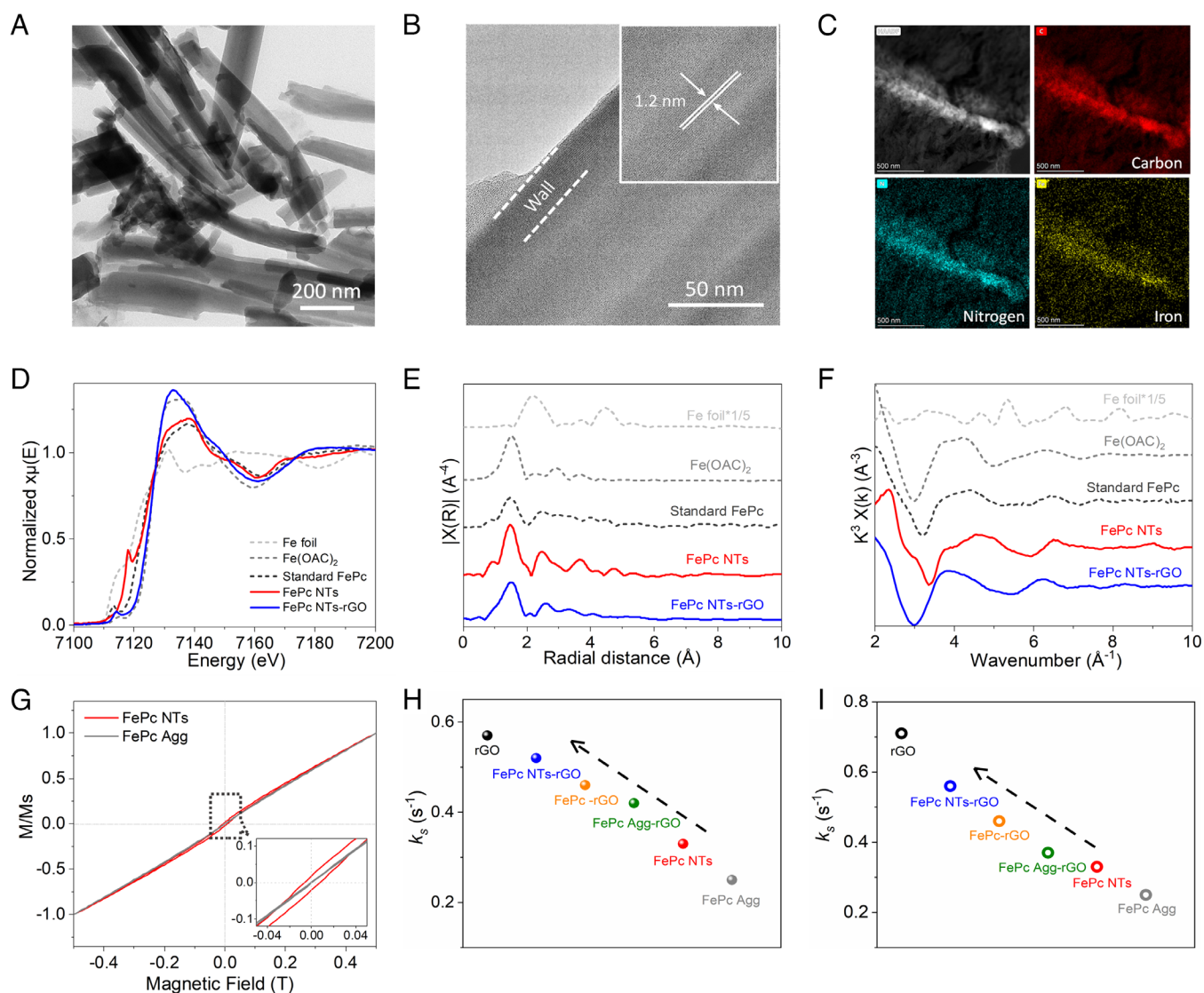

Fig. 1. Low (*A*) and high (*B*) resolution TEM images of FePc NTs. (*C*) Typical dark-field TEM image of FePc NTs-rGO with the corresponding elemental mapping images by EDX analysis. (*D*) Fe K-edge XANES data of FePc NTs and FePc NTs-rGO, and the data of Fe foil, Fe(OAc)$_2$ and FePc standards are included for comparison. Corresponding Fourier transformed EXAFS data in R-space (*E*) and k-space (*F*). (*G*) SQUID magnetizations of FePc NTs and FePc Agg conducted at 5 K. *Inset* shows a zoom on the central region. Kinetic constants of interfacial electron transfer on various samples probed using 1 mM Ru (NH$_3$)$_6$Cl$_3$/0.1 M KCl (*H*) and 1 mM K$_3$Fe(CN)$_6$/0.1 M KCl (*I*).

Fig. S1 *A and B*). The high-resolution image (Fig. 1*B*) indicates a lattice fringe with an interlayer distance of 1.2 nm by the (110) plane of FePc NTs, and the FePc NTs are uniformly dispersed on rGO (Fig. 1*C* and *SI Appendix*, Fig. S1 *C and D*). The lattices of FePc NTs were reflected by X-ray diffraction (XRD, *SI Appendix*, Fig. S2*A*) patterns. Typically, the peaks at 7.3°, 9.5°, and 18.5° are indexed to the (100), (102), and (302) planes of FePc molecules assembling into β-phase (JCPDS Card No. 14-0926) (23). Upon FePc NTs anchoring onto rGO, only graphene characters are observed. This is possibly because the mono-dispersion led to a relatively a low loading of FePc NTs. Nevertheless, the Raman spectra of FePc NTs-rGO clearly show the combined scattering features of E_g, B_{1g}, and B_{2g} bands of FePc NTs with D-/G-bands of graphene (*SI Appendix*, Fig. S2*B*) (24). The UV–visible (UV–vis) spectra of FePc NTs-rGO also present the typical B- and Q-bands of Pc complexes (*SI Appendix*, Fig. S3). The X-ray photoelectron spectroscopy (XPS, *SI Appendix*, Figs. S4 and S5) surveys reveal the coexistence of Fe and N elements of FePc NTs-rGO. In the core electron surveys, the Fe $2p_{3/2}$ peak of FePc NTs is positioned at 711.2 eV. Upon anchoring onto rGO, this peak shifts to 711.7 eV accompanied with the shift of N 1 s peak from 398.5 eV to 398.9 eV. Such slight shifts suggest an efficient electron communications between FePc NTs and rGO (25). To further characterize the structures of the as-synthesized samples, X-ray absorption near-edge structure (XANES) and Fourier transformed-extended X-ray absorption fine structure (FT-EXAFS) analysis were conducted. As shown in Fig. 1*D*, FePc NTs exhibit the absorption edge close to the FePc standard. There is a slight shift to higher energy in FePc NTs-rGO. This is consistent with the XPS results for partial electrons moving from FePc NTs to rGO. Besides, an intensive pre-edge peak of FePc NTs is observed at ~7,117 eV for 1*s* to 4p_z transition with simultaneous ligand-to-metal charge transfer, which strongly indicates the planar geometry of FePc NTs. Their D_{4h} symmetry is even more perfect than the FePc standard, as indicated by the decrease of the 1*s* to 4p_z transition, and the emergence of 1*s* electrons transiting into 3*d*-4*d* mixed orbitals (~7,112 eV) (26). With the presence of rGO, the D_{4h} symmetry of FePc NTs is also decreased. The FT-EXAFS data of FePc NTs and FePc NTs-rGO suggest that their first and outer sphere coordination shells are both well consistent with the FePc standard and are clearly distinct from the precursor of Fe(OAc)$_2$ (Fig. 1 *E* and *F*). These results demonstrate the successful synthesis of FePc complexes with NTs morphology and anchored onto rGO in a mono-dispersion state.

To investigate the potential aggregation effects on the electrocatalytic performance of FePc, we included two control samples for comparison, which are randomly aggregated FePc (directly using pristine FePc powders, denoted as FePc Agg) and molecularly dispersed FePc. For FePc Agg, it has nanosheet-like morphology and stack tightly (*SI Appendix*, Fig. S6). The sample was intentionally mixed with rGO in isopropanol, which is a poor solvent for FePc, to maintain the pristine morphologies in the final hybrid (denoted as FePc Agg-rGO). Both the XRD patterns, Raman and UV–vis spectra confirm the formation of FePc Agg with graphene layers hybrid, and FePc Agg has α-phase (*SI Appendix*, Figs. S7 and S8). The molecularly dispersed FePc was achieved in a good solvent of *N, N*-dimethylformamide (DMF), which interacted with rGO following the previous work (27) (the as-derived sample is denoted as FePc-rGO). The SEM/TEM, XRD, and Raman data of FePc-rGO only exhibit the graphene characters (*SI Appendix*, Figs. S9 and S10), while the UV–vis spectra present the typical B- and Q-bands of FePc (*SI Appendix*, Fig. S11). This should reflect the well dispersion of FePc on rGO without clear agglomeration. The Fe contents of FePc Agg-rGO and FePc-rGO were controlled at

1.4×10^{-6} mol mg^{-1} and 0.96×10^{-6} mol mg^{-1}, respectively, according to ICP measurements, which are close to the data of FePc NTs-rGO.

With the morphological evolution of FePc, some structural properties of FePc are significantly tuned. In a magnetization measurement (Fig. 1*G*), the hysteresis loop of FePc NTs exhibits a ferromagnetic-like curve with some remanence and coercivity, but there are no such signals for FePc Agg under the same conditions. The similar phenomenon was reported previously in the FePc-based assemblies (28). which suggests the anisotropy of FePc molecules and their assemblies. It is very possible that the alignment of FePc molecule with NT morphology is more ordered compared to that of FePc Agg. Correspondingly, FePc NTs-rGO presents higher specific surface area and structural stability than FePc Agg-rGO and FePc-rGO (*SI Appendix*, Figs. S12–S14). In addition, the evolution of electrical conductivity is noted (Fig. 1 *H* and *I*). The electron transfer property of each sample was tested by both outer-sphere [i.e., 1 mM Ru(NH$_3$)$_6$Cl$_3$/0.1 M KCl, *SI Appendix*, Fig. S15] and inner-sphere (i.e., 1 mM K$_3$[Fe(CN)$_6$]/0.1 M KCl, *SI Appendix*, Fig. S16) probes based on the Laviron analysis (29). FePc Agg exhibits relatively low redox constant (k_s) of interfacial electron transfer in both Ru(NH$_3$)$_6^{3+}$ and Fe(CN)$_6^{3-}$ based probing. The k_s values are clearly increased on FePc NTs. The incorporation of rGO can facilitate electron transfer of all samples; the k_s values on FePc NTs-rGO clearly remain more significant than those on FePc Agg-rGO, as well as FePc-rGO.

ORR Performance. The electrocatalysis of ORR was conducted by the linear scanning voltammograms (LSVs) combining with a rotating ring-disk electrode (RRDE) equipment in 0.1 M KOH (all potentials are referred to the reversible hydrogen electrode, RHE, if not specified). As shown in Fig. 2*A*, the bottom graph includes the disk currents and the upper graph includes the corresponding ring currents. On FePc NTs-rGO, the onset (E_{onset}) and half-wave ($E_{1/2}$) potentials of ORR reach 0.97 V and 0.88 V, respectively. These are apparently higher than the ones observed on FePc Agg-rGO and FePc-rGO and are even superior to the data of commercial Pt/C catalyst. In the selected potential range, the HO$_2^-$ yields on FePc NTs-rGO are around 5% according to the ring-to-disk current ratio. Such ORR efficiency is comparable to those on Pt/C catalyst and is also significantly improved compared to the case of FePc Agg-rGO and FePc-rGO (Fig. 2*B*). The analysis of turnover frequencies (TOFs, Fig. 2*C* and *SI Appendix*, Fig. S17 and Table S2) of Fe sites also supported that FePc NTs-rGO is more active than FePc Agg-rGO and FePc-rGO. Temperature programmed desorption (*SI Appendix*, Fig. S18) measurements suggest that FePc NTs-rGO has relatively high chemical affinity with O$_2$ (30, 31). In the absence of rGO, the pristine FePc NTs also exhibit much improved ORR performance compared to FePc Agg (*SI Appendix*, Fig. S19). To verify the catalytic role of FePc NTs, 10 mM KSCN was added into 0.1 M KOH during ORR on FePc NTs-rGO to intentionally coordinate with Fe sites. As expected, clear loss in catalytic current is observed, suggesting that the Fe sites serve as the main active sites (*SI Appendix*, Fig. S20). To evaluate the electrocatalytic durability, the LSVs of FePc NTs-rGO were continuously conducted for 5,000 cycles, which shows a negligible loss in both potential and current density, and the morphology of FePc NTs-rGO is well remained after the durability test (*SI Appendix*, Fig. S21). We fabricated a custom zinc–air battery to conduct a preliminary assessment of the practical viability of FePc NTs-rGO. The stabilized open-circuit voltage of the zinc–air battery powered by FePc NTs-rGO attained 1.44 V, surpassing that achieved by the Pt/C driven battery (1.39 V, *SI Appendix*, Fig. S22). Accordingly, the FePc NTs-rGO-based
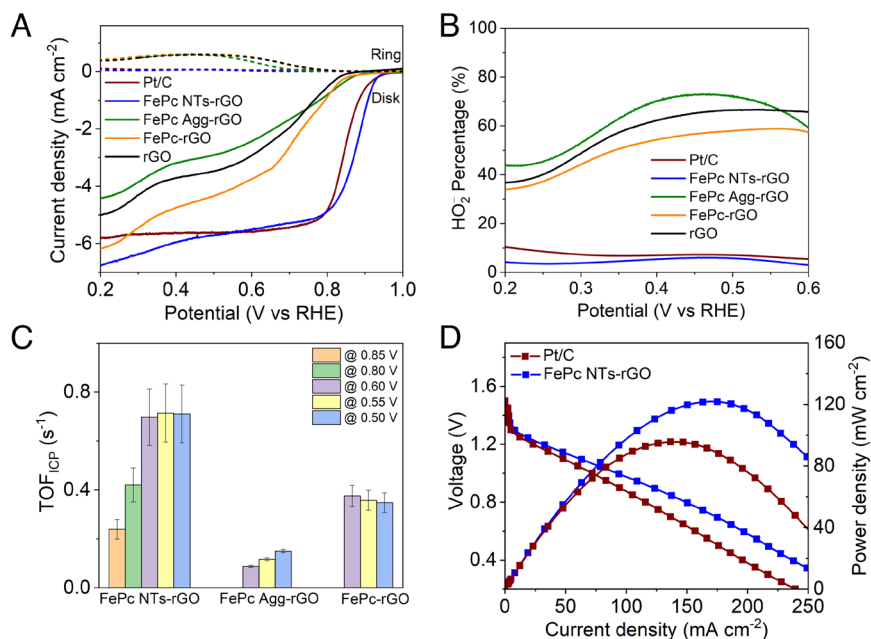
Fig. 2. (*A*) RRDE measurements recorded with FePc NTs-rGO, FePc Agg-rGO, FePc-rGO, rGO, and 20% Pt/C in O_2 saturated 0.1 M KOH, 1600 rpm, 10 mV s^{-1}. During the measurements, the potential of ring electrode was kept constant at 1.07 V. (*B*) The HO_2^- percentage of ORR on various catalysts, derived from the corresponding RRDE measurements. (*C*) TOFs of Fe sites derived from the Koutecky–Levich analysis. (*D*) A polarization curve and corresponding power density plot of the zinc-air battery using FePc NTs-rGO as the cathode catalyst compared with the battery using Pt/C catalyst.

battery achieved superior discharge performance and the peak power density of 120.3 mW cm^{-2}, outperforming the Pt/C-based counterpart (93.1 mW cm^{-2}, Fig. 2*D*).

In alkaline solutions, the electrocatalysis of ORR could involve ISET/OSET mechanisms (14). The ISET mechanism promotes the direct/series 4e$^-$ transfer pathway, while the OSET mechanism promotes the yield of stable peroxide (14, 32). Thus, the redox features of H_2O_2 (or/and its anion form), as the probing test, were investigated on the various samples. On the pristine FePc NTs (*SI Appendix*, Fig. S23*A*), there is significant current of H_2O_2 reduction reaction (HRR) in the ORR potential range. However, HRR is trivial on FePc Agg with a very low onset potential approaching 0.5 V. Note that their HRR and ORR potentials are highly consistent. In the cases of FePc Agg-rGO and FePc-rGO, HRR currents are also not significant (*SI Appendix*, Fig. S23*B*), where H_2O_2 thus can be stabilized during the ORR events. It is very possible that the OSET mechanism is involved in the ORR electrocatalyzed by FePc Agg-rGO and FePc-rGO. Such a mechanism facilitates the formation of H_2O_2 from O_2 solvated by hydroxide species, and the active sites are occupied by hydroxide species to stabilize the generated H_2O_2 (32). In contrast, there is significant HRR currents emerging on FePc NTs-rGO. The onset potential approaches 0.9 V being consistent with the one for ORR, suggesting that H_2O_2 cannot be stabilized during the ORR electrocatalysis on FePc NTs-rGO. Thus, either series or direct four-electron transfer ORR events occur on FePc NTs-rGO, which is consistent with the above RRDE measurements. This suggests the possible ISET mechanism for ORR occurring on FePc NTs-rGO, where O_2 is directly adsorbed onto Fe sites to operate ORR (33).

Mechanistic Investigations. Since the Fe sites of FePc NTs-rGO are identified as the main ORR active sites, their redox properties can be closely related to the catalytic performance. As indicated by the cyclic voltammograms (CVs), the redox features of the based catalytic system change with the variation of morphologies. For FePc-rGO (Fig. 3 *A* and *D*), there is a pair of redox peaks, assigned

to the Fe$^{2+/3+}$ pair emerging around 0.8 V in 0.1 M KOH under a N_2 atmosphere (13). At the same potential, a very clear reduction peak occurs upon purging O_2 as the ORR event occurs. This should suggest that the redox-mediated mechanism is operative toward ORR on FePc-rGO.(11, 14) For FePc Agg-rGO (Fig. 3 *B* and *E*), the CV is featureless under a N_2 atmosphere without clear redox of Fe$^{2+/3+}$ pair. We thus speculate that ORR should directly occur on the Fe^{2+}–N sites, while the kinetics of interfacial electron transfer could be slow. For FePc NTs-rGO (Fig. 3 *C* and *F*), the redox of Fe$^{2+/3+}$ pair at around 0.8 V is much more significant compared to the above two cases. The XANES data suggest the same Fe oxidation state in FePc-rGO and FePc NTs-rGO (*SI Appendix*, Fig. S24). However, the ORR peak potential emerges around 0.9 V, which is more positive than the potential of Fe^{3+}/Fe^2 redox. Clearly, in this case, the redox-mediated mechanism is not operative, and ORR should commence with a Fe^{3+}–N state.

The Pourbaix diagram of samples was then tested at various pH values within the alkaline range. Both the redox potentials of Fe$^{2+/3+}$ pair of FePc-rGO and FePc NTs-rGO increase with the decrease of solution pH values (*SI Appendix*, Figs. S25 and S26), indicating that the HO$^-$ ions coupled redox of Fe$^{2+/3+}$ pair. The Pourbaix linear slope of FePc-rGO is fitted to be 60 mV pH^{-1} (Fig. 3*G*), suggesting that each Fe$^{2+/3+}$ redox event couples with one HO$^-$ ion. This is typical for FePc based on ORR, namely, the reduction of one Fe^{3+} site into Fe^{2+} site detaches one HO$^-$ ion, leaving an open site at the axial position of FePc for the chemisorption of O_2 to commence the catalysis (10, 34). In contrast, the Pourbaix linear slope of FePc NTs-rGO increases to 79 mV pH^{-1}, suggesting that each Fe$^{2+/3+}$ redox event couples with more than one HO$^-$ ions. For a free-standing FePc molecule, it is possible that both planar sides could interact with HO$^-$ ion. Upon anchoring onto rGO with the common face-to-face stacking, it should generate the steric effects at one side of FePc and blocks the chemisorption of HO$^-$ ions. In contrast, in the assembled FePc NTs, since there are no chemical bonds between neighboring molecules, we speculate that it could leave certain space to improve
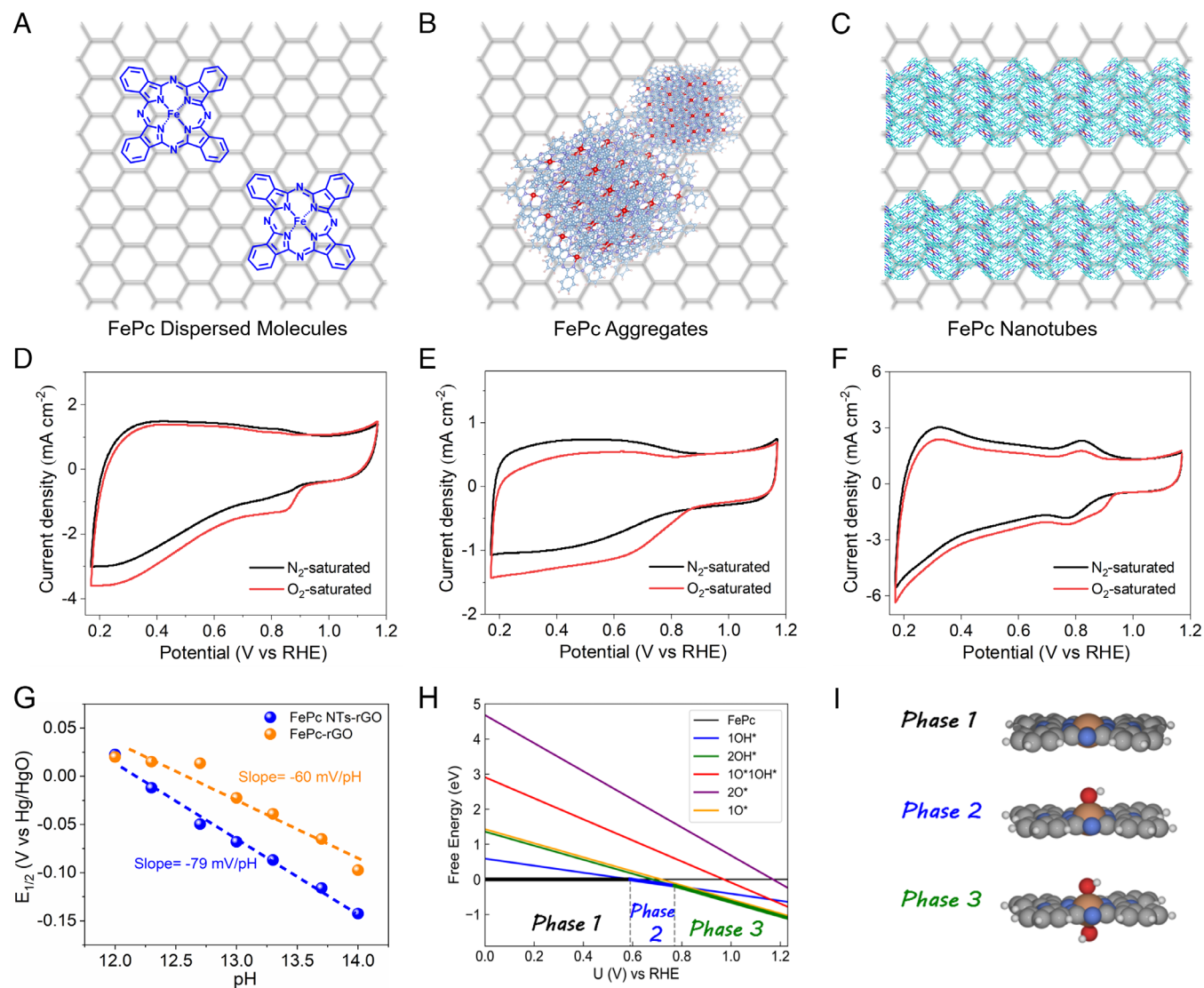
Fig. 3. Schemes show the morphologies of FePc-rGO (*A*), FePc Agg-rGO (*B*), and FePc NTs-rGO (*C*). Corresponding CVs of FePc-rGO (*D*), FePc Agg-rGO (*E*), and FePc NTs-rGO (*F*) conducted in N_2/O_2 saturated 0.1 M KOH, respectively, 50 mV s^{-1}. (*G*) Pourbaix diagram of FePc-rGO and FePc NTs-rGO for the redox of Fe centers. (*H*) Surface phase diagram of FePc as a function of applied potentials. (*I*) Geometrical structures of three most stable phases of FePc.

the chemisorption of HO$^-$ ions at both planar sides of FePc. The ORR electrocatalysis on FePc NTs should commence by replacing one HO$^-$ ion with O_2, namely, on a Fe^{3+}–N state attaching with one HO$^-$ ion. In in situ electrochemical Raman measurements of FePc NTs-rGO (*SI Appendix*, Fig. S27), the typical FePc vibration kept emerging from high to low potentials (35), verifying the stable molecular structure in catalysis. Note that the peak intensity of in-plane Fe–N$_4$ stretching vibration at 591 cm^{-1} is also almost unchanged, indicating the durable planar geometry of FePc. This could support the Pourbaix data that with operating ORR at one side of the FePc plane, there were oxygen species adsorbing at the other side of FePc to maintain its planar geometry (35). Accordingly, through the DFT calculations, we verified the surface phase diagram of FePc at various potentials (Fig. 3 *H* and *I*). At relatively high potentials, two *OH species chemisorb at both sides of FePc planar surface (phase 3). This reflects the experimental Pourbaix observation. With approaching moderate potentials, only one *OH specie leaves to chemisorb onto FePc, resulting in the formation of FePc–OH (phase 2). Further decrease of potential makes FePc unoccupied by any *OH adsorbates (phase 1).

These results verify that both FePc and FePc–OH can serve as the active sites for ORR.

To gain insights into the ORR activity of FePc and FePc–OH, we further elucidate the atomic-level reaction mechanism. Fig. 4*A* shows the projected density of states of *d*-orbitals of a Fe site (valence electrons $3d^6 4s^2$) in FePc, which reveals a distribution of six *d*-electrons at an intermediate spin state, leading to a total magnetic moment of 2 μB. This observation shows that two *4s* electrons are transferred to the neighboring N ligands, which is well consistent with the above spectral analytical results that Fe site in FePc is at +2 oxidation state. Upon chemisorption of one *OH specie onto FePc, the d_{yz} orbital of spin-down channel becomes unoccupied, resulting in a total magnetic moment of 3 μB (Fig. 4*B*). This indicates an +3 oxidation state of Fe site in FePc–OH, which is also consistent with our Pourbaix results. As the change of Fe oxidation state may influence the ORR performance, we compared the free energy diagrams on FePc and FePc–OH. It shows that the intrinsic activity of FePc is limited by over strong binding of ORR intermediates on FePc (Fig. 4*C*). This results in an overpotential of 0.64 V, corresponding to the
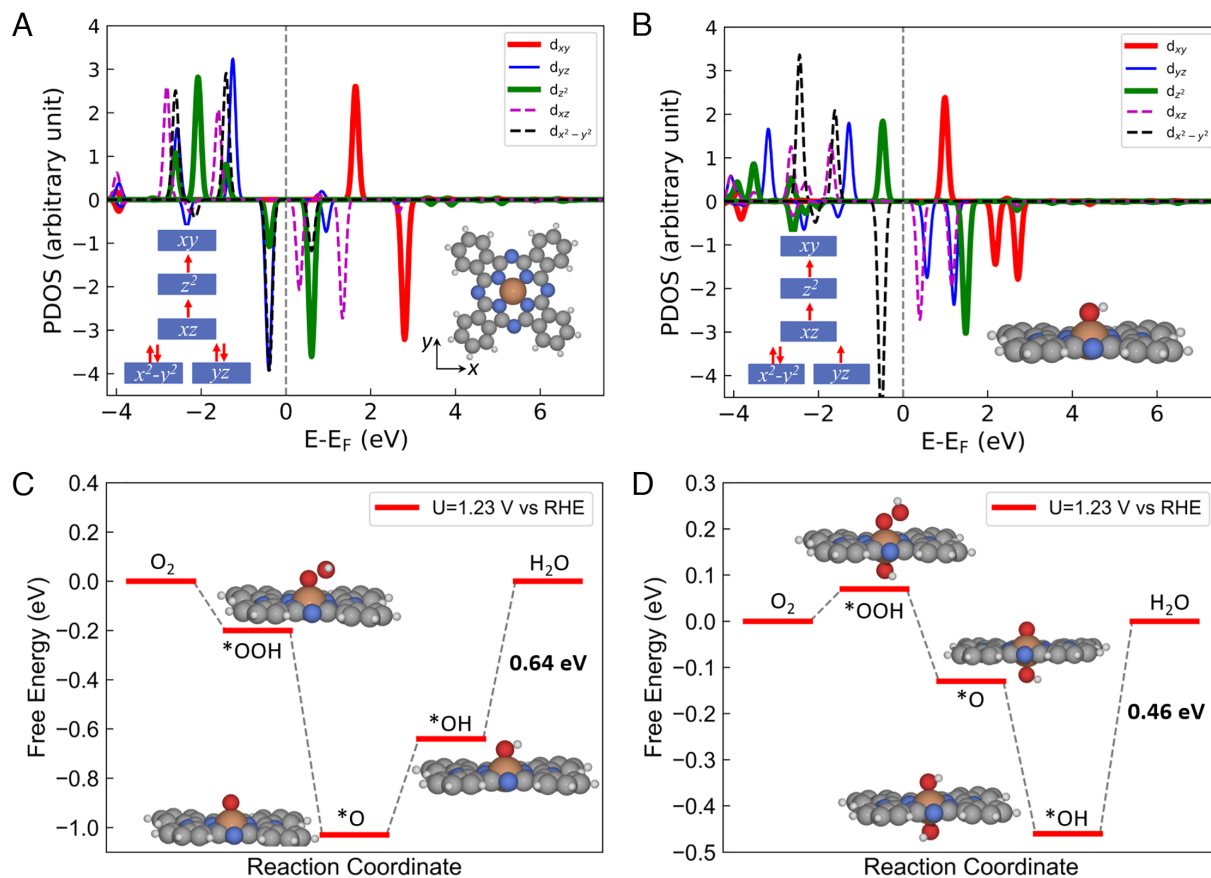
Fig. 4. Density of states projected onto the d orbitals of Fe atoms in FePc (*A*) and FePc with an adsorbed OH*, i.e., FePc–OH (*B*). Free energy diagrams of ORR on FePc (*C*) and FePc–OH (*D*).

electroreduction of OH* into H_2O. In contrast, the attachment of OH* species with FePc appropriately weakens the binding of those intermediates on the Fe site. As a result, the overpotential of ORR on FePc–OH decreases to 0.46 V (Fig. 4*D*), indicating that the HO–Fe^{3+}–N moiety has the excellent intrinsic ORR activity.

Conclusion

In summary, we have successively synthesized FePc NTs anchoring onto rGO based on a straightforward ethylene glycol-assisted solvothermal method. The as-derived FePc NTs-rGO is structurally stable and electrically conductive. Toward the electrocatalysis of ORR, it exhibits much improved four-electron transfer activity compared to random aggregates and molecular dispersion of FePc and becomes superior to commercial Pt/C catalysts. Unlike the conventional FePc, where the operation of ORR on a Fe^{2+}–N state follows the redox-mediated mechanism, the ORR potential is tuned to above the redox potential of $Fe^{2+/3+}$ sites on FePc NTs. Further Pourbaix analysis indicates that nanotube architecture promotes the coupling of HO^- ions with the redox of $Fe^{2+/3+}$ sites, and thus leads to a HO–Fe^{3+}–N moiety serving as the ORR active sites under the turnover condition. Such a moiety appropriately weakens the chemisorption of ORR intermediates on the Fe sites compared to the Fe^{2+}–N state, and is thus intrinsically more active. The employed strategy opens a new avenue for the development of large-scale production of efficient electrocatalysts for electrochemical energy conversion and storage systems.

Materials and Methods

All the chemicals are analytical reagents and were used as received. The rGO was synthesized by a modified Hummers' method to first derive GO, which was followed by the hydrothermal reduction of GO. The FePc NTs were synthesized by an ethylene glycol-assisted solvothermal method. The combination of rGO and FePc NTs was realized in DMF by heating at 80 °C for 12 h. The ORR performance was evaluated by the RRDE measurements at the ambient condition. The other electrochemical measurements were also conducted at the ambient condition using a common three-electrode system. DFT calculations, using the BEEF-vdW exchange and correlation functional at the generalized gradient approximation, were carried out to optimize the structures and unveil the electronic structures. The detailed information is presented in *SI Appendix*.

Author affiliations: [a]Innovation Center for Chemical Science, College of Chemistry, Chemical Engineering and Materials Science, Soochow University, Suzhou 215006, China; [b]Jiangsu Key Laboratory of New Power Batteries, Jiangsu Collaborative Innovation Center of Biomedical Functional Materials, School of Chemistry and Materials Science, Nanjing Normal University, Nanjing 210023, China; [c]Department of Physics, Southern University of Science and Technology, Shenzhen 518055, China; [d]Jiangsu Key Laboratory of Advanced Negative Carbon Technologies, Soochow University, Suzhou, Jiangsu 215123, China; and [e]State Key Laboratory of Analytical Chemistry for Life Science, School of Chemistry and Chemical Engineering, Nanjing University, Nanjing 210023, China

1. S. Chu, A. Majumdar, Opportunities and challenges for a sustainable energy future. *Nature* **488**, 294–303 (2012).
2. T. Zhou, N. Zhang, C. Wu, Y. Xie, Surface/interface nanoengineering for rechargeable Zn–air batteries. *Energy Environ. Sci.* **13**, 1132–1153 (2020).
3. M. Shao, Q. Chang, J.-P. Dodelet, R. Chenitz, Recent advances in electrocatalysts for oxygen reduction reaction. *Chem. Rev.* **116**, 3594–3657 (2016).
4. X. Wang et al., Review of metal catalysts for oxygen reduction reaction: From nanoscale engineering to atomic design. *Chem* **5**, 1486–1511 (2019).
5. D. Y. Chung, J. M. Yoo, Y.-E. Sung, Highly durable and active Pt-based nanoscale design for fuel-cell oxygen-reduction electrocatalysts. *Adv. Mater.* **30**, 1704123 (2018).
6. Y. Chen et al., Atomic-level modulation of electronic density at cobalt single-atom sites derived from metal-organic frameworks: Enhanced oxygen reduction performance. *Angew. Chem. Int. Ed. Engl.* **60**, 3212–3221 (2021).
7. G. Zhang et al., A general route via formamide condensation to prepare atomically dispersed metal–nitrogen–carbon electrocatalysts for energy technologies. *Energy Environ. Sci.* **12**, 1317–1325 (2019).
8. H. Xu, D. Cheng, D. Cao, X. C. Zeng, A universal principle for a rational design of single-atom electrocatalysts. *Nat. Catal.* **1**, 339–348 (2018).
9. K. Chen et al., Iron phthalocyanine with coordination induced electronic localization to boost oxygen reduction reaction. *Nat. Commun.* **11**, 4173 (2020).
10. J. H. Zagal, M. T. M. Koper, Reactivity descriptors for the activity of molecular MN4 catalysts for the oxygen reduction reaction. *Angew. Chem. Int. Ed. Engl.* **55**, 14510–14521 (2016).
11. S. Mukherjee et al., A biosynthetic model of cytochrome c oxidase as an electrocatalyst for oxygen reduction. *Nat. Commun.* **6**, 8467 (2015).
12. J. P. Collman, S. Ghosh, A. Dey, R. A. Decréau, Y. Yang, Catalytic reduction of O2 by cytochrome c using a synthetic model of cytochrome c oxidase. *J. Am. Chem. Soc.* **131**, 5034–5035 (2009).
13. A. van der Putten, A. Elzing, W. Visscher, E. Barendrecht, Redox potential and electrocatalysis of O_2 reduction on transition metal chelates. *J. Electroanal. Chem.* **221**, 95–104 (1987).
14. N. Ramaswamy, U. Tylus, Q. Jia, S. Mukerjee, Activity descriptor identification for oxygen reduction on nonprecious electrocatalysts: Linking surface science to coordination chemistry. *J. Am. Chem. Soc.* **135**, 15443–15449 (2013).
15. M. N. Jackson, C. J. Kaminsky, S. Oh, J. F. Melville, Y. Surendranath, Graphite conjugation eliminates redox intermediates in molecular electrocatalysis. *J. Am. Chem. Soc.* **141**, 14160–14167 (2019).
16. C. J. Kaminsky, S. Weng, J. Wright, Y. Surendranath, Adsorbed cobalt porphyrins act like metal surfaces in electrocatalysis. *Nat. Catal.* **5**, 430–442 (2022).
17. J. Mei, N. L. C. Leung, R. T. K. Kwok, J. W. Y. Lam, B. Z. Tang, Aggregation-induced emission: Together we shine, united we soar! *Chem. Rev.* **115**, 11718–11940 (2015).
18. J. Gu, Z. Li, Q. Li, From single molecule to molecular aggregation science. *Coord. Chem. Rev.* **475**, 214872 (2023).
19. A. Kumar, K. Sun, X. Duan, S. Tian, X. Sun, Construction of dual-atom Fe via face-to-face assembly of molecular phthalocyanine for superior oxygen reduction reaction. *Chem. Mater.* **34**, 5598–5606 (2022).
20. S. Ren et al., Catalyst aggregation matters for immobilized molecular CO2RR electrocatalysts. *J. Am. Chem. Soc.* **145**, 4414–4420 (2023).
21. M. Gilbert Gatty et al., Hopping versus tunneling mechanism for long-range electron transfer in porphyrin oligomer bridged donor-acceptor systems. *J. Phys. Chem. B* **119**, 7598–7611 (2015).
22. U. K. Ghorai et al., Scalable production of cobalt phthalocyanine nanotubes: Efficient and robust hollow electrocatalyst for ammonia synthesis at room temperature. *ACS Nano* **15**, 5230–5239 (2021).
23. A. S. Milev, N. Tran, G. S. Kamali Kannangara, M. A. Wilson, I. Avramov, Polymorphic transformation of iron-phthalocyanine and the effect on carbon nanotube synthesis. *J. Phys. Chem. C* **112**, 5339–5347 (2008).
24. U. K. Ghorai et al., Raman spectroscopic observation of gradual polymorphic transition and phonon modes in CuPc nanorod. *J. Phys. Chem. C* **121**, 6323–6328 (2017).
25. Z. Li et al., The marriage of the FeN4 moiety and MXene boosts oxygen reduction catalysis: Fe 3d electron delocalization matters. *Adv. Mater.* **30**, 1803220 (2018).
26. Q. Jia et al., Experimental observation of redox-induced Fe–N switching behavior as a determinant role for oxygen reduction activity. *ACS Nano* **9**, 12496–12505 (2015).
27. J. Wang et al., Linkage effect in the heterogenization of cobalt complexes by doped graphene for electrocatalytic CO2 reduction. *Angew. Chem. Int. Ed. Engl.* **58**, 13532–13539 (2019).
28. A. N. Filippin et al., Self-assembly of the nonplanar Fe(III) phthalocyanine small-molecule: Unraveling the impact on the magnetic properties of organic nanowires. *Chem. Mater.* **30**, 879–887 (2018).
29. E. Laviron, General expression of the linear potential sweep voltammogram in the case of diffusionless electrochemical systems. *J. Electroanal. Chem.* **101**, 19–28 (1979).
30. J. Woo et al., Fe-N/C catalysts with tunable mesoporous structures and carbon layer numbers reveal the role of interlayer O_2 activation. *EES Catal.* **1**, 62–73 (2023).
31. J. H. Kim et al., A general strategy to atomically dispersed precious metal catalysts for unravelling their catalytic trends for oxygen reduction reaction. *ACS Nano* **14**, 1990–2001 (2020).
32. N. Ramaswamy, S. Mukerjee, Influence of inner- and outer-sphere electron transfer mechanisms during electrocatalysis of oxygen reduction in alkaline media. *J. Phys. Chem. C* **115**, 18015–18026 (2011).
33. A. J. Bard, Inner-sphere heterogeneous electrode reactions. Electrocatalysis and photocatalysis: The challenge. *J. Am. Chem. Soc.* **132**, 7559–7567 (2010).
34. A. Alsudairi et al., Resolving the iron phthalocyanine redox transitions for ORR catalysis in aqueous media. *J. Phys. Chem. Lett.* **8**, 2881–2886 (2017).
35. J. Wei et al., Probing the oxygen reduction reaction intermediates and dynamic active site structures of molecular and pyrolyzed Fe–N–C electrocatalysts by in situ raman spectroscopy. *ACS Catal.* **12**, 7811–7820 (2022).